ADVANCED OPTICAL MATERIALS
www.advopticalmat.de

# Driving Micro-Objects Using Optical Force due to Fluorescence Emission From Molecules

*Syoji Ito,* Takayuki Nanno, Takahiro Kaji, Mamoru Tamura, Takuya Iida, and Hiroshi Miyasaka*

**Emission of fluorescence in a specific direction generates an optical force in the opposite direction of the emission by the momentum conservation raw. This "emission force" can induce the directional transportation of small objects anisotropically emitting fluorescence from molecules in the objects only by photo-irradiation without any spatio-temporal control of light field. To demonstrate the movement by the emission force, we fabricated dye-doped cylinder-shaped polymer micro-objects (PMOs) with gold thin films on their top surfaces. The single PMOs in water on a glass substrate, the side surfaces of which were facing to the substrate, were photoexcited with a continuous wave visible (532 nm) laser. The dyes in a PMO emitted strong fluorescence toward the non-coated end (bottom) of the micro-cylinder due to the reflection by the gold thin film on the top. The individual motions of the PMOs under photoexcitation are detected with fluorescence microscopy. Analysis of the trajectories of the PMOs confirmed that the anisotropic fluorescence emission led to the transportation of the PMOs in the opposite direction of the fluorescence. The emission force acting on the PMO is quantitatively evaluated through computational simulation considering the emission force and Brownian motion.**

## 1. Introduction

Radiation pressure (Optical force) acting on an object was first detected in the end of the 19th century by two research groups of Levedev[1] and Nichols and Hull.[2] As the momentum of single photon is too small, it was practically not possible to manipulate small particles by light until the development of lasers that can emit highly intense light beams. Ashkin and co-workers demonstrated optical manipulation of microparticles using lasers beams: optical transportation using slightly focused laser beams in 1970[3] and single-beam laser tweezing on the basis of optical gradient force in 1986.[4]

Optical force acting on a small particle that can be regarded as a point dipole can be simply classified into three terms, scattering, absorption, and gradient forces. The scattering and absorption forces act toward the propagation direction of photons, while the gradient force acts along the spatial intensity gradient of light field. Under the condition that the refractive index of a particle is larger than that of the surrounding medium, the gradient force pushes the particle toward the direction of increasing intensity of light. By utilizing these optical forces, various micromanipulations can be achieved, such as atom/molecule trapping in vacuum at low temperature,[5–8] selective transportation and spatial arrangement of quantum dots [9,10] and plasmonic nanoparticles[11] in fluids, fabrication of microscopic structures with nanoparticles using gradient-force optical tweezer,[12,13] and measurement of micro-mechanical properties of motor proteins.[14,15]

Optical micro-manipulation is generally achieved by transferring the momentum of photons of a relatively intense laser beam to micro-objects. Meanwhile, when a micro-object anisotropically emits fluorescence photons, an optical force as a reaction of the fluorescence emission is generated and acts on the objects, resulting in the motion of the object toward the opposite direction of the photon emission. In such micro-mechanical motion due to fluorescence emission, the direction and speed of micromotion are determined by the emission property of a micro-object. Hence even under a spatially uniform photoexcitation, a directional motion is expected and, the motion can be controlled by changing emission property of the micro-object by several approaches, such as replacing the fluorescent emitters (dyes) in the

S. Ito, T. Nanno, M. Tamura, H. Miyasaka
Division of Frontier Materials Science and Center for Promotion of Advanced Interdisciplinary Research, Graduate School of Engineering Science
Osaka University
1–3 Machikaneyama-cho, Toyonaka, Osaka 560-8531, Japan
E-mail: sito@chem.es.osaka-u.ac.jp
T. Kaji
Advanced ICT Research Institute
National Institute of Information and Communications Technology (NICT)
588-2 Iwaoka, Nishi-ku Kobe 651-2492, Japan
T. Iida
Department of Physics, Graduate School of Science
Osaka Metropolitan University
1–2, Gakuen-cho, Naka-ku, Sakai, Osaka 599-8570, Japan
S. Ito, M. Tamura, T. Iida
Research Institute for Light-induced Acceleration System (RILACS)
Osaka Metropolitan University
1–2, Gakuen-cho, Naka-ku, Sakai, Osaka 599-8570, Japan
The ORCID identification number(s) for the author(s) of this article can be found under https://doi.org/10.1002/adom.202403546



**DOI: 10.1002/adom.202403546**

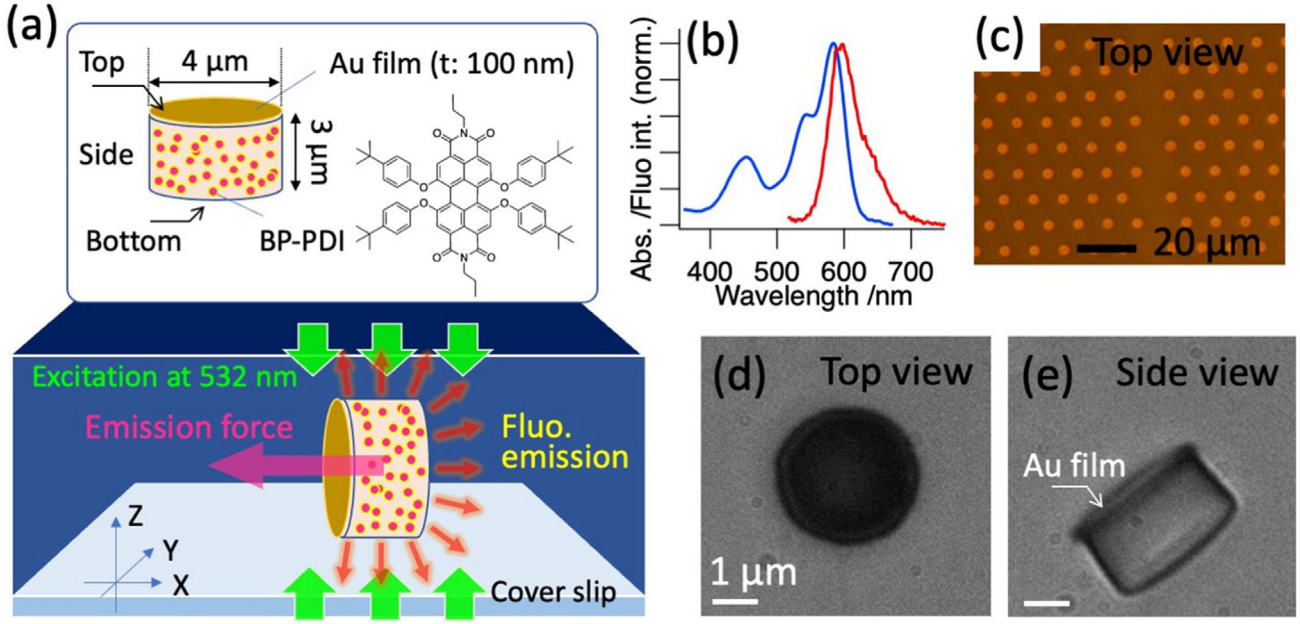


**Figure 1.** a) Schematic illustration of the PMO driven by emission force in the present study. b) Normalized absorption and fluorescence spectra of BPPDI in a PMMA film. c) Metallurgical micrograph of dye-doped PMOs on a Si substrate fabricated by photolithography. d,e) Optical transmission micrographs of a dye-doped PMO, d) top and e) side views.

micro-object with those exhibiting different spectroscopic property, modifying the geometry of the micro-object, and increasing/decreasing the reflectance at the surface(s) of the micro-object. In the present study, we aim to demonstrate this new micro-mechanical motion on the basis of the optical force due to the emission from a micro-object itself. For this purpose, we have prepared dye-doped polymer micro-objects (PMOs) exhibiting anisotropic fluorescence emission and evaluated their individual motions under photoexcitation.

## 2. Results and Discussion

### 2.1. Motion of PMO Emitting Fluorescence Photons under Intense Photoexcitation

**Figure 1** schematically illustrates fluorescence emission of a perylenediimide derivative with butylphenoxy groups (BPPDI) embedded in a PMO and resultant optical force (called emission force hereinafter). The detailed procedure for fabricating the PMOs of poly(methyl methacrylate) (PMMA) which anisotropically emitted fluorescence is described in Figure S1 (Supporting Information). One of the end-faces (top and bottom) of the PMMA microcylinder was covered with a 100-nm thick gold film that reflects fluorescence photons from the BPPDI in the PMO. The end face with Au film will be called "top face" hereinafter. Without the Au film, the PMO exhibits symmetric fluorescence emission along the axis of the cylinder shape (*x*-axis in Figure 1a). Owing to this symmetric emission along the *x*-axis, optical forces acting the two end-faces of the micro-object along the *x*-axis cancel each other and resultant optical force is zero. Therefore, the anisotropic fluorescence emission realized by the Au film on the top face plays a crucial role for directional driving of the PMO by the emission force. As a result of reflection by the Au film, fluorescence photons from the BPPDI come out from the side and bottom faces as illustrated in Figure 1a. Considering the rotational symmetry of the side face, the sum of optical force along the *y*-*z* plane of Figure 1a is also zero due to its rotational symmetry. While the optical force parallel to the X axis acts anisotropically because of the anisotropic fluorescence emission. Hence the micro-object moves parallel with the *x*-axis. Because the fluorescence emission of individual dyes is a dipole emission showing spatially anisotropic emission pattern, the orientation of embedded BPPDI affects the emission force acting the PMOs. To evaluate the orientation of the embedded dyes, we measured fluorescence intensity of a 3-μm PMMA film containing BPPDI under photoexcitation with linearly polarized 532-nm laser at different polarization directions. The measurement revealed that the orientation of the dyes is random in the objective plane (*x*-*y* plane in Figure 1a) of the microscope. To obtain the information of the orientation of the dyes with respect to the *z*-axis in Figure 1a, we also conducted widefield focus and defocus imaging for a thinner PMMA film. The widefield imaging indicated that the orientation of the dyes is three-dimensionally random in the PMMA film. The detailed results of the measurements are shown in Figure S3 (Supporting Information).

A drop of water including the cylinder-shaped PMOs was sandwiched with a pair of well cleaned coverslips with keeping the thickness of the liquid film of 0.5 mm using a punched 0.5-mm silicone rubber sheet. One of the PMOs on the cover slip was photoexcited under optical microscope and the motion due to the anisotropic fluorescence emission was observed by fluorescence microscopy as shown in Figure 1a. The details of the optical setup for the photoexcitation and microscopic imaging are described in the Experimental Section.

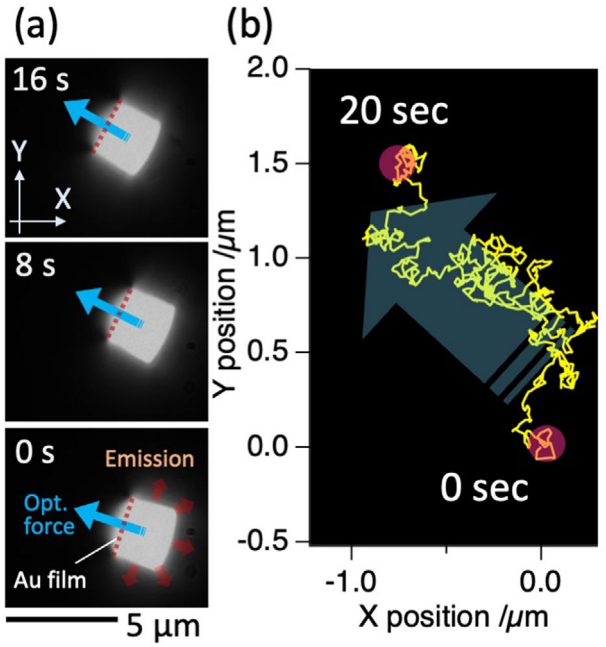


**Figure 2.** a) Fluorescence images of a cylindrical PMO containing BPPDI under photoexcitation at 532 nm at 2400 $Wcm^{-2}$ (bottom) at the time origin (just after the start of photoexcitation), (middle) after 8 s, and (top) after 16 s from the start of the photoexcitation. b) Corresponding detailed trajectory of the centroid of the fluorescence image of the PMO for 20 s.

**Figure** 2a shows a time-course of the fluorescence image for one of the dye-doped PMOs under photoexcitation at 532 nm at 2400 W $cm^{-1}$. The position of Au film and the direction of fluorescence emission are indicated in the images. As shown by the images in Figure 2a, the micro-object moved to the direction of upper left. Figure 2b shows the corresponding trajectory at every 30 ms of the centroid of the micro-object for 20 s under photoexcitation. The movie for this motion is provided as a Video S1 (Supporting Information) (5 times speed). The trajectory shows overall unidirectional motion from 0 to 20 s, indicating that the emission force induced the directional motion of the micro-object. However, the positional fluctuations of the centroid and the lateral angle of the micro-object were also observed in the corresponding fluorescence video, suggesting that the random motion due to the thermal (Brownian) motion is superimposed on the directional motion driven by the emission force. During the 20 s observation, the fluorescence intensity of the PMO did not drastically decrease, indicating that the photobleaching of the dyes in the PMO was not remarkable in the observation period. However, the fluorescence intensity somewhat decreased in 20 s, which was evaluated with a PMMA film containing BPPDI at the same concentration, the result of which is shown in Figure S3 (Supporting Information).

### 2.2. Comparison of the Motions of PMOs Containing BPPDI with Those Containing MG

To differentiate the Brownian motion from the directional one by the emission force, we tracked lateral motions of PMOs at very low (0.37 $Wcm^{-2}$) excitation intensities. In this fluorescence imaging at the low excitation intensity, the 532-nm laser was used only for fluorescence excitation and the emission force due to the fluorescence was almost negligible. On the other hand, stronger emission force acts on the PMO at the high intensity photoexcitation (2400 $Wcm^{-2}$) as shown above. **Figure** 3a shows trajectories of PMOs under the high and very low photoexcitation intensities. In both cases, the PMOs started their motions from the origin (X = 0, Y = 0). The PMO under the weak photoexcitation exhibited almost ideal random walk; the position of the object distributed within ≈ ±500 nm from the origin (X = 0, Y = 0). In contrast, the trajectory under the high photoexcitation intensity shows a biased diffusion from the origin to the positive X direction. These results support ascribing the directional motion to the emission force. Note that the direction of biased diffusion due to emission force depends on the orientation of a PMO. The PMO whose trajectory is shown in Figure 2a as red line started its motion parallel to the *x*-axis with a configuration that the top face with Au film directs to the positive X region.

To further investigate the effect of emission force on the trajectory in terms of nonradiative relaxation of (heat dissipation from) embedded dyes, we fabricated PMOs containing malachite green (MG) at the same concentration as the BPPDI. The molar absorption coefficient, $\epsilon$, of BPPDI at 532 nm was estimated to be 29 000 $cm^{-1}$ $M^{-1}$ from literatures,[16,17] while that of MG to be 8000 $cm^{-1}$ $M^{-1}$.[18] The fluorescence quantum yield of MG and BPPDI in PMMA solid was estimated through the comparison of fluorescence intensity with rhodamine 6G (R6G) in PMMA film at a determined absorbance on the basis of a reported fluorescence quantum yield of R6G in PMMA (0.75).[19] As shown in Figure 3b where normalized fluorescence spectra of R6G, BPPDI, and MG in the PMMA films are exhibited, no emission was observed for MG in PMMA film. The fluorescence quantum yield of MG in the PMMA film was determined to be <0.01, indicating that almost all photon energy absorbed by MG is converted to heat in the PMMA solid. On the other hand, fluorescence quantum yield of BPPDI in the PMMA solid was estimated almost unity (>0.95), expecting much less photothermal effect.

Figure 3c shows trajectories (tracked positions) for 20 s of 4 single PMOs containing MG at the high intensity photoexcitation (2400 $Wcm^{-2}$) as green solid circles. The trajectories for 4 PMOs with BPPDI under weak (0.37 $Wcm^{-2}$) excitation condition are also plotted as blue solid circles in the same figure in the same manner. In these plots, connecting lines between successive tracked positions are omitted for visibility. The histograms of X and Y positions for the PMOs are also plotted at the bottom (X distribution) and the right side (Y distribution) of the trajectories. As predicted by the very low fluorescence quantum yield of MG, the intense photoexcitation of the PMOs with MG led to heat generation through nonradiative relaxation of MG after photoexcitation. As a result, diffusion coefficient of the PMOs with MG under the intense photoexcitation increased, then the PMOs with MG exhibited wider XY distribution of the tracked position in Figure 3c compared with PMOs with BPPDI under very weak photoexcitation.

To further, statistically analyzing the motions of the PMOs under photoexcitation, we plotted mean square displacement

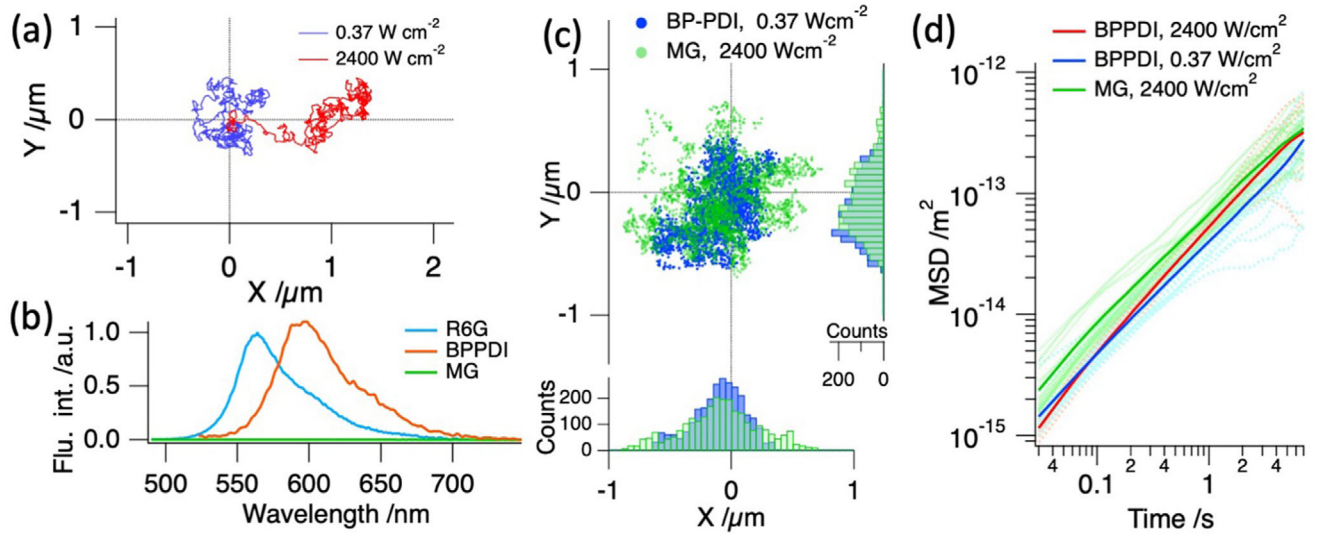


**Figure 3.** a) Trajectories for 20 s of PMOs containing BPPDIs under the high (red solid line, at 2400 $Wcm^{-2}$) and very low (blue solid line, at 0.37 $Wcm^{-2}$) photoexcitation intensities. The exposure time of the imaging was 30 ms for both cases. b) Fluorescence spectra of R6G, BPPDI, and MG in PMMA film excited at 462 nm normalized on the basis of fluorescence quantum yield. c) Tracked positions of PMOs with MG under strong excitation (green circles, at 2400 $Wcm^{-2}$) and those with BPPDI under very weak excitation (blue dots, 0.37 $Wcm^{-2}$). Corresponding histograms of the X and Y positions of the trajectories are also plotted at the bottom (X) and the right side (Y); the colors of the bars are corresponding to those of the XY distributions of the tracked positions. d) MSD-t plots of 20 dye-doped PMOs for each condition: PMOs containing BPPDIs photoexcited at 2400 and at 0.37 $Wcm^{-2}$, and PMOs containing MGs photoexcited at 2400 $Wcm^{-2}$. MSD-t plots for individual PMOs are shown in dotted lines, light red: BPPDI at 2400 $Wcm^{-2}$, light blue: BPPDI at 0.37 $Wcm^{-2}$, and light green: MG at 2400 $Wcm^{-2}$. Solid lines of red, blue, and green show accumulated (averaged) MSD-t plots over the 20 PMOs for each condition.

(MSD) as a function of time for the three photoexcitation conditions. Figure 3d shows double-logarithmic MSD versus time (MSD-t) plots which were accumulated (averaged) over 20 PMOs for each photoexcitation condition: PMO with BPPDI photoexcited at 2400 $Wcm^{-2}$, PMO with BPPDI photoexcited at 0.37 $Wcm^{-2}$, and PMO with MG photoexcited at 2400 $Wcm^{-2}$. Individual MSD-t plots for the 20 PMOs under each condition are also shown as light-colored dotted lines in the same figure. The accumulated MSD-t plot for the PMOs with BPPDI excited at 0.37 $Wcm^{-2}$ exhibits monotonic increase with a slope of unity. Hence the motion can be regarded as normal diffusion (Brownian motion). The accumulated MSD-t plot for PMOs with MG under intense photoexcitation also shows monotonic increase with a slope of unity, parallel to the accumulated MSD-t plot for the PMOs with BPPDI under weak excitation with some offset. The result indicates the motions of the PMOs with MG under intense photoexcitation can also be regarded as normal diffusion, but the lateral diffusion coefficient is different between the two Brownian motions. The difference in the MSD values between the blue and green lines corresponds to the difference in each lateral diffusion coefficient. On the other hand, the accumulated MSD-t plot for the PMOs with BPPDI under intense photoirradiation (solid red line) clearly exhibits a slope lager than these two MSD-t plots (blue and green solid lines), indicating that the motion of the red line can be classified as super diffusion ascribable to the biased motion due to emission force. The MSD-t plots for PMOs with BPPDI at weak and intense excitations should also be discussed in terms of photothermal effect. If the Brownian (thermal) motion of a PMO under intense photoexcitation is enhanced by temperature elevation through photothermal conversion by BPPDI and/or gold film, the MSD-t plot for the PMO with BPPDI under intense excitation should start at a higher MSD value as the PMOs with MG (green line in Figure 3d). However, the MSD-t plots in Figure 3d for the PMOs with BPPDI under intense (red line) and very weak (blue line) excitations show almost same MSD values around the time origin (at 30 ms). This indicates the PMOs with BPPDI under weak and intense excitations show almost same Brownian motions. In addition to the Brownian motion, the PMOs with BPPDI under intense excitation underwent the biased motion due to the emission force. The effect of this biased motion becomes obvious with increasing time in the MSD-t plot; the difference between the red and blue lines increases with time as shown in Figure 3d. The result, comparable MSD values around time origin between the PMOs with BPPDI under weak and intense photoexcitation, indicates negligible photothermal effect due to the nonradiative relaxation of BPPDI nor the absorption of the 532-nm laser by the Au film.

### 2.3. Numerical Investigation of the Motions of PMOs under Photoexcitation

To elucidate the contribution of emission force to the motion of the PMO with BPPDI, we conducted a series of numerical simulations. The details of the simulations are described in the Experimental Section. **Figure 4a** shows the positional distributions of the centroids of single PMOs on the *x*-*y* plane at the time $t$ = 20 s in the absence and presence of emission force, $F_{em}$ = 0, 10, and 20 fN. The motion of the single PMO started at the

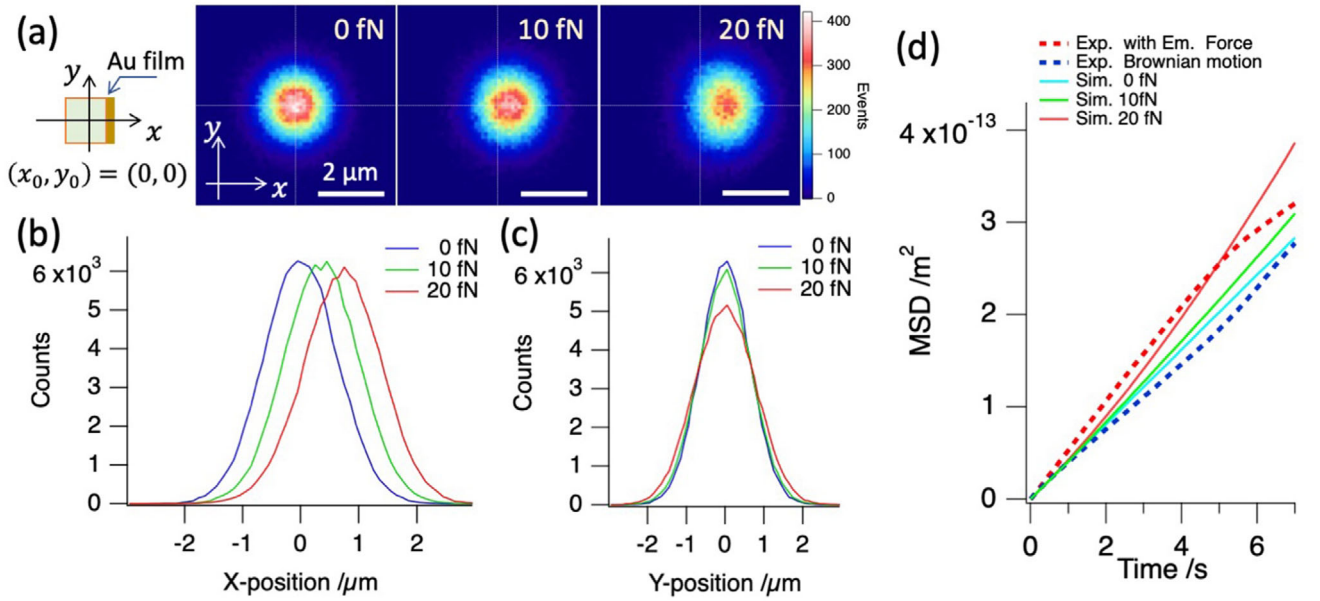


**Figure 4.** a) 2D (on the *x*-*y* plane) distributions of the lateral position (centroid) of the PMO in the absence (0 fN) and presence (10 and 20 fN) of emission force. The simulations started at the origin ($x_0$, $y_0$) = (0, 0) with the orientation of the PMO shown in the left. b,c) Positional distribution of PMO along (b) X and (c) Y axes for the simulation results shown in (a). d) MSD-t plots of PMOs obtained through experiment (solid lines) and simulation (dotted lines) in the absence (blue lines) and presence (red lines) of emission force.

origin ($x = 0$, $y = 0$) and, the emission force acts perpendicular to the Au film as shown in Figure 1. The positional changes of the centroid and orientation of a PMO were tracked for 20 s at the interval of 0.01 s. Without emission force, the PMO underwent Brownian motion (normal diffusion), leading to the rotationally symmetric distribution of the centroid that can be reproduced by 2D gauss function. While in the presence of emission force, $F_{em}$ = 10 and 20 fN, the 2D distribution of the centroid shifted toward positive X region and its symmetry with respect to the *y*-axis was broken as shown in the Figure. This spatial shift of the 2D distribution along the *x*-axis well reproduces the experimental result shown in Figure 3a. Figure 4b,c respectively show the *x* and *y* distributions of the centroid position shown in Figure 4a. The peak position of the *x*-distribution shifts toward +X direction with increasing emission force. While the peak position of the Y distribution (ca. y = 0) does not change, but the peak intensity decreases, and the width becomes slightly wider. This wider distribution can be ascribed to longer MSD due to emission force and is consistent with the experimental result shown in Figure 3d.

Figure 4d shows MSD-t plots obtained through the experiment and simulation. It should be noted here that the diffusion coefficient of the PMO without emission force is lower than that determined only from the viscosity of water owing to the drag of the surface of cover slip. In this simulation, we introduced an effective viscous drag to reproduce the lateral and rotational diffusion of the PMO. The details of this effective diffusion coefficient are described in Figure S2 (Supporting Information). The MSD-t plot for the PMO in the presence of emission force (red lines) clearly shows a larger slope than that without emission force (blue lines) and, the simulation considering an emission force of 20 fN well reproduced the experimental result. We can therefore conclude here that the PMOs with BPPDI under photoexcitation at 2400 $Wcm^{-1}$ generated ≈20 fN as its emission force by fluorescence.

### 2.4. Analysis of the Motions of PMOs in Terms of Moving Direction

Although the larger slope than unity of the log-log MSD-t plot for PMOs with BPPDI under the high photoexcitation intensity indicated that the motions of the PMOs were biased by emission force, the analysis on MSD does not provide the direct correlation between the orientation of a PMO and the direction of motion due to the emission force. For more quantitative evaluation of the above correlation, we calculated the inner product, $IP_i = n_i \cdot \Delta r_i = |n_i|\,|\Delta r_i|\cos\theta$, between the normal unit vector of the top surface with the Au film, $n_i$, and the *i*-th motional vector within the exposure time (30 ms), $\Delta r_i = r_{i+1} - r_i$. Here, $r_i$ is the position vector of a PMO at *i*-th video frame. It should be noted here that the individual PMOs have three degrees of freedom in its rotational motions: 1) rotation along angle theta (in **Figure 5**a) on the x-y plane, 2) that on the x-z plane in Figure 1a, and 3) that around the center axis of the cylinder. The rotational motion 1) has already been mentioned above. The rotation 2) was not observed for the individual PMOs with their side faces on the glass substrate because it was restricted owing to the aspect ratio of the PMO. Regarding the rotation 3), as already discussed in the section 2.1, optical force along the *y*-*z* plane of Figure 1a is zero owing to the rotational symmetry of the fluorescence emission from the side face. We hence do not consider the rotation 3) because it does not affect the motion of the PMOs in the present study.

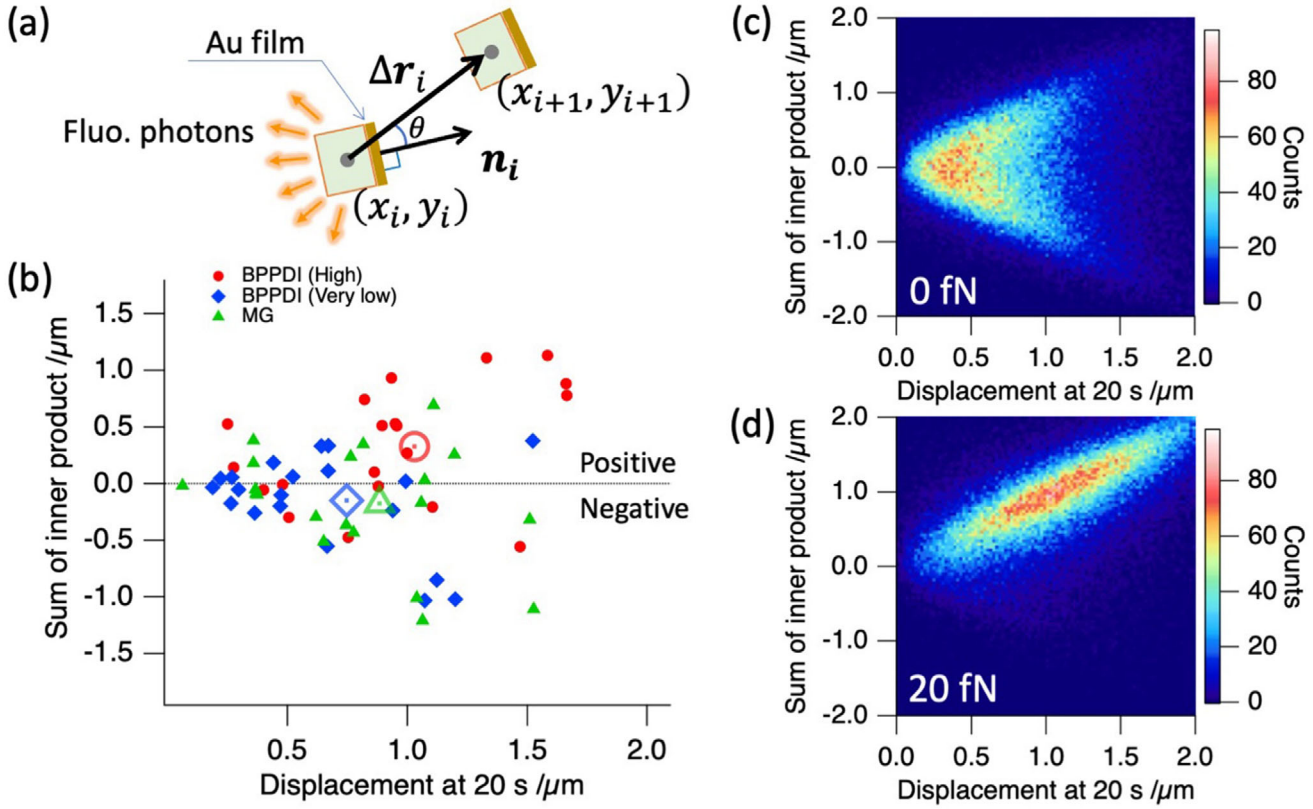


**Figure 5.** a) Definition of vectors, $n_i$ and $\Delta r_i$, for the analysis of the correlation between the orientation of a PMO and the direction of motion due to the emission force through the calculation of the inner product, $IP_i = n_i \cdot \Delta r_i = |n_i| |\Delta r_i| \cos\theta$. b) Correlation plots between the sum of the inner product of every 30-ms steps for 20 s and the displacement at 20 s for the motions of single PMOs under the following three photoexcitation conditions: (red solid circles) micro-objects containing BPPDI under the high (2400 $Wcm^{-2}$) excitation intensity, (blue solid squares) those with BPPDI under the very low (0.37 $Wcm^{-2}$) excitation intensity, and (green solid triangles) those with MG under the high (2400 $Wcm^{-2}$) excitation intensity. The relatively large open circle, square, and triangle are corresponding averaged values. c,d) Simulated distribution of the sum of the inner product versus the displacement from the initial position for c) $F_{em} = 0$ and d) 10 fN at 20 s, where the inner product was added for every time step of simulation.

The analysis using inner product is schematically illustrated in Figure 5a. The inner product exhibits a maximum value, $|\Delta r_i|$, when the PMO moves parallel to the normal unit vector, $n_i$, in the same direction ($\theta = 0$). The value of the inner product decreases with an increase in the angle, $\theta$, between the vectors, $\Delta r_i$ and $n_i$. Figure 5b shows the correlation plots between the sum of the inner product, $\sum_{i=1}^{667} IP_i$, and the displacement at 20 s for 20 individual trajectories under the following three experimental systems: 1) micro-objects containing BPPDI under the high (2400 $Wcm^{-2}$) and 2) the very low (0.37 $Wcm^{-2}$) excitation intensities and 3) those containing MG under the high (2400 $Wcm^{-2}$) excitation intensity. In addition, to investigate how the correlation should be distributed, we conducted a series of computations that simulated the 2D motion of a micro-object in the presence of emission force and Brownian motion. Figure 5c,d show simulated distributions of the sum of the inner product as a function of the displacement from the initial position in the absence (Figure 5c, $F_{em} = 0$ fN) and presence (Figure 5d, $F_{em} = 20$ fN) of emission force. In the simulation, $n(t) \cdot (r(t + \delta t) - r(t)) = F_{em}\delta t/\xi_{\parallel} + \delta r_{\parallel}$ was summed for every time step. To evaluate the distribution, the plot area was discretized by 100 × 100 segments with the width $\delta h = 0.02$ μm and $\delta v = 0.04$ μm for horizontal and vertical axes of plot. In each segment, the number of simulations resulting the corresponding correlation was counted in all simulation samples *N*s. As shown in Figure 5c, the random diffusion of Brownian motion shows the symmetric distribution for positive and negative area, whereas in Figure 5d, the emission force displaces the micro-objects for positive area. Therefore, in the experimental result (Figure 5b), the correlation plot for 1) including the contributions of emission force and Brownian motion locates in the positive area of Figure 5b. On the other hand, the motions of 2) and 3) are due to only Brownian motion; thus, its randomness distributes the correlation plots for 2) and 3) for positive and negative area in the equal probability. The positive value of averaged $\sum n_i \cdot \Delta r_i$ for the motions of 1) indicates the directional motions of the micro-objects along $n_i$ due to the emission of BPPDI. On the other hand, almost zero values of averaged $\sum n_i \cdot \Delta r_i$ for the motions of 2) and 3) can be assigned to Brownian motion. In addition, the averaged displacement at 20 s of 1) is 1.5 times as large as that of 2) owing to the biased motion due to the emission force. The similar behavior could be confirmed also in the simulation result in Figure 5c,d; the distribution in Figure 5c resembles a vertically symmetric triangle with respect to the zero line of the vertical axis, while the distribution of Figure 5d extended for more oblique direction. Comparing the motions of 2) and 3),

the averaged displacement of 3) is larger than that of 2), which can be ascribed to the temperature elevation due to the efficient photothermal conversion of MG increased the diffusion coefficient of the micro-objects as already discussed on the data in Figure 3d.

## 3. Conclusion

Cylindrically shaped polymer micro-objects containing fluorescent dyes, BPPDI, were fabricated by using photolithographic technique. The one end of each cylindrical micro-object was covered with Au film of 100-nm thick so that the micro-objects exhibited anisotropic fluorescence emission under photoexcitation at 532 nm. The individual micro-objects in water were driven by the optical force due to the anisotropic fluorescence emission toward the opposite direction of the emission. Because the micro-object underwent Brownian motion as well, the trajectories of the micro-objects were the superimpose of unidirectional motion driven by the emission force and random thermal motion. On the basis of computational simulations, the emission force acting on the micro-objects was estimated to be ≈10-20 fN under the 532 nm photoexcitation.

Thus, we have successfully realized the microscopic mechanical motion of the small objects driven by the emission of photons from the object, like a rocket driven through the emission of particles. In this approach, the motion is determined by anisotropic emission behavior from a micro-object under spatially uniform photoexcitation intensity. This demonstration may lead to variety of micro-motion by controlling the emission behavior of a micro-object through several approaches such as the modification of its geometry, using another dye showing different spectroscopic properties, and facet-selective control of optical properties. We foresee that the achievement of this study can provide a new series of photo-mechanical microsystems driven by simple photoexcitation condition. Toward the control of further elaborate mechanical micro-motions, different microstructures and different molecular systems are under investigation.

## 4. Experimental Section

*Optical Setup*: The individual cylinder-shaped PMOs were photoexcited under optical microscope and their motions due to the anisotropic fluorescence emission were observed by fluorescence microscopy. A continuous wave (CW) fiber laser with triple wavelength emission at 355, 532, and 1064 nm (3-band CW laser, OXIDE) was used as the excitation source in the present study; the 532 nm linearly polarized output was selected for the excitation of the PMOs. The CW green laser beam was split into two beams with orthogonally linear polarizations by a polarizing beam splitter. The diameter of one of the beams was expanded by a factor of three with a beam expander. This beam was introduced into an inverted optical microscope (IX70, Olympus) through a pair of plano-convex lenses and focused by an oil-immersion objective lens (UPLanFLN 100X, NA 1.30, Olympus) to achieve upward widefield illumination. The spot size of the beams with a Gaussian shape at the sample position under the microscope was ≈40 μm in diameter. The other beam was slightly focused by a plano-convex lens with a focal length of 300 mm for downward illumination of the sample. The relative angle between the polarizations of the two linearly polarized counter-propagating beams was adjusted to be 90 degrees at the sample plane. Because the diameters of the two excitation beams were much larger than the size of the micro-object, homogeneous illumination was achieved. Each excitation intensity was set to 1200 $Wcm^{-2}$ then the coaxially counter-propagating illumination balanced absorption and scattering forces in the vertical direction. The total excitation intensity was 2400 $Wcm^{-2}$ at the sample plane. Compared with general setup for optical tweezers where a laser beam is focused to a small spot the size of which is comparable to its wavelength, the illumination size for this experiment is much larger. The optical gradient force, therefore, is negligible in the present illumination configuration.

A drop of the water suspension of the cylinder-shaped PMOs was confined in a sample cell consisting of two cover slips and a 50-μm thick silicone-rubber spacer with a square hole of ≈10 × 10 $mm^2$. The motion of the PMOs in water under photoexcitation was observed by the inverted optical microscope in fluorescence imaging mode using a monochromatic CCD camera (INFINITY3-1URM, Lumenera). The detection wavelength range corresponding to the fluorescence band of the BPPDI, ≈540 – 780 nm, was ensured by using optical long-pass (LP03-532RU-25, Semrock) and short-pass (BSP01-785R-25, Semrock) filters. Note that as the excitation intensity (2400 $Wcm^{-2}$) was quite high compared with ordinary fluorescence imaging, suitable neutral density (ND) filters were used for decreasing the fluorescence intensity from the micro-object down to an appropriate intensity level within the dynamic range of the CCD camera.

*Numerical Simulation*: Dynamics of optically driven micro-object was simulated based on the Brownian dynamics method. The time-evolution was expressed by,[20]

$$r\ (t+\delta t) = r\,(t) + \frac{F_{\mathrm{em}}}{\xi_{\parallel}}\delta t n\,(t) + \delta r_{\parallel} n\,(t) + \delta r_{\perp} e_z \times n\,(t) \tag{1}$$

$$n\ (t+\delta t) = n\,(t) + \delta\psi e_z \times n\,(t) \tag{2}$$

where $\boldsymbol{r}$ is the position of micro-object, $t$ is the time, $F_{\mathrm{em}}$ is the optical force due to the emission, $n$ is the direction vector parallel for the center axis of cylindrical shape of micro-object, $e_z$ is the unit vector for $z$-axis, $\delta r_{\parallel}$ and $\delta r_{\perp}$ are the random variation of transrational motion for parallel and perpendicular direction, and $\delta\psi$ is the random variation of angle in radians around $z$-axis, during the single time-step with the width $\delta t$ = 10 μs. In the simulation, it was assumed that $n$ kept parallel for $x$-$y$ plane and the optical force $\boldsymbol{F}_{\mathrm{em}}$ acted for the direction of $\boldsymbol{n}$, i.e., $F_{\mathrm{em}} = \boldsymbol{F}_{\mathrm{em}} \bullet \boldsymbol{n} = |\boldsymbol{F}_{\mathrm{em}}|$. For the random variations, their mean value must be zero and their mean square satisfies $\langle \delta r_{\parallel}^2 \rangle = 2D'_{\parallel}\delta t$, $\langle \delta r_{\perp}^2 \rangle = 2D'_{\perp}\delta t$, and $\langle \delta\psi^2 \rangle = 2D_{\mathrm{R}}\delta t$ in the 2D motion. To evaluate the diffusion coefficient, the expressions for the oblate spheroid was employed,[21]

$$D_{\parallel} = \frac{k_B T}{8\pi\eta a}\frac{\left(2-p^2\right)G\,(p)-1}{1-p^2} \tag{3}$$

$$D_{\perp} = \frac{k_B T}{16\pi\eta a}\frac{\left(2-3p^2\right)G\,(p)+1}{1-p^2} \tag{4}$$

$$D_{\mathrm{R}} = \frac{3k_B T}{16\pi\eta a^3}\frac{\left(2-p^2\right)G\,(p)-1}{1-p^4} \tag{5}$$

where $k_{\mathrm{B}}$ is the Boltzmann constant, $T$ = 298 K is the temperature of medium, $\eta$ = 0.89 mPa s is the viscosity of medium, $p = b/a$ is the aspect ratio, $a$ = 1.5 μm and $b$ = 2 μm are the semiaxes of oblate, and $G\,(p) = \arctan(\sqrt{p^2-1})/\sqrt{p^2-1}$ for $p > 1$ ($G(p)$ for $p < 1$ is also mentioned in[21]. Using the diffusion coefficient, the friction coefficient for parallel direction is given as $\xi_{\parallel} = k_B T/D_{\parallel}$ . The final time of simulation was $t_{\mathrm{fin}}$ = 20 s. The position of micro-object was recorded in every 0.01 s. Here, the simulation using the diffusion coefficients of equations (3) and (4) yields the much larger displacement compared with the actual experiments. Originally, a friction due to the interaction between the micro-object and glass surface must decrease the diffusion coefficients. To consider this effect, we modified the diffusion coefficients as $D'_{\parallel} = f_{\mathrm{m}}\ D_{\parallel}$ and $D'_{\perp} = f_{\mathrm{m}}\ D_{\perp}$ with the modification factor $f_{\mathrm{m}}$. The value of $f_{\mathrm{m}}$ was determined by the comparison with experiment (See Supporting Information).

To discuss the statistic behavior of micro-object, we carried out the simulation repeatedly. The number of simulation samples were $N_s = 10^5$. As an initial condition, the object in all samples were located at the origin and oriented for *x*-direction, i.e., $r(0) = (0, 0, 0)$ and $n(0) = (1, 0, 0)$ .

## Supporting Information

Supporting Information is available from the Wiley Online Library or from the author.

## Acknowledgements

This work was supported by JSPS KAKENHI grant numbers JP23H01923 (SI), JP21KK0092 (SI), JP22K19007 (SI), JP21H04640 (SI), JP21H04964 (TI and SI), JP21H01889 (HM), JP23H04594 (MT), JP24K08282(MT) and JST-Mirai Program Grant Number JPMJMI21G1(TI and SI).

## Conflict of Interest

The authors declare no conflict of interest.

## Data Availability Statement

The data that support the findings of this study are available from the corresponding author upon reasonable request.

## Keywords

fluorescence, optical emission force, optical force, optical manipulation, photomechanical microsystems

Received: December 27, 2024
Revised: March 10, 2025
Published online:

[1] P. Lebedew, *Ann. Phys.* **1901**, *311*, 433.
[2] a) E. F. Nichols, G. F. Hull, *Phys. Rev. (Series I)* **1903**, *17*, 26; b) E. F. Nichols, G. F. Hull, *Phys. Rev. (Series I)* **1903**, *17*, 91.
[3] A. Ashkin, *Phys. Rev. Lett.* **1970**, *24*, 156.
[4] A. Ashkin, J. M. Dziedzic, J. E. Bjorkholm, S. Chu, *Opt. Lett.* **1986**, *11*, 288.
[5] A. Ashkin, *Phys. Rev. Lett.* **1970**, *25*, 1321.
[6] S. Chu, J. E. Bjorkholm, A. Ashkin, A. Cable, *Phys. Rev. Lett.* **1986**, *57*, 314.
[7] C. Gabbanini, A. Fioretti, A. Luchesini, S. Gozzini, M. Mazzoni, *Phys. Rev. Lett.* **2000**, *84*, 2814.
[8] A. Ashkin, *IEEE J. Sel. Top. Quantum Electron.* **2000**, *6*, 841.
[9] T. Iida, H. Ishihara, *Phys. Rev. Lett.* **2003**, *90*, 057403.
[10] K. Inaba, M. Ashida, T. Iida, K. Imaizumi, K. Katayama, M. Ichimiya, H. Ishihara, T. Itoh, *Phys. Stat. Sol.* **2006**, *243*, 3829.
[11] S. Ito, H. Yamauchi, M. Tamura, S. Hidaka, H. Hattori, T. Hamada, K. Nishida, S. Tokonami, T. Itoh, H. Miyasaka, T. Iida, *Sci. Rep.* **2013**, *3*, 3047.
[12] S. Ito, H. Yoshikawa, H. Masuhara, *Appl. Phys. Lett.* **2001**, *78*, 2566.
[13] S. Ito, H. Yoshikawa, H. Masuhara, *Appl. Phys. Lett.* **2002**, *80*, 482.
[14] S. M. Block, L. S. B. Goldstein, B. J. Schnapp, *Nature* **1990**, *348*, 348.
[15] K. Kitamura, M. Tokunaga, A. H. Iwane, T. Yanagida, *Nature* **1999**, *397*, 129134.
[16] U. Selig, P. Nuernberger, V. Dehm, V. Settels, M. Gsänger, B. Engels, F. Würthner, T. Brixner, *ChemPhysChem* **2013**, *14*, 1413.
[17] E. Avellanal-Zaballa, G. Durán-Sampedro, A. Prieto-Castañeda, A. R. Agarrabeitia, I. García-Moreno, I. López-Arbeloa, J. Bañuelos, M. J. Ortiz, *Phys. Chem. Chem. Phys.* **2017**, *19*, 13210.
[18] M. Taniguchi, J. S. Lindsey, *Photochem. Photobiol.* **2018**, *94*, 290.
[19] R. Reisfeld, R. Zusman, Y. Cohen, M. Eyal, *Chem. Phys. Lett.* **1988**, *147*, 142.
[20] J. R. Rothenbuhler, J.-R. Huang, B. A. DiDonna, A. J. Levinec, T. G. Mason, *Soft Matter* **2009**, *5*, 3639.
[21] M. Hoffmann, C. S. Wagner, L. Harnau, A. Wittemann, *ACS Nano* **2009**, *3*, 3326.